# Effect of pre-existing defects in the parent fcc phase on atomistic mechanisms during the martensitic transformation in pure Fe

## A molecular dynamics study

Karewar, S.; Sietsma, J.; Santofimia Navarro, Maria

**DOI**
10.1016/j.actamat.2017.09.049

**Publication date**
2018

**Document Version**
Final published version

**Published in**
Acta Materialia

**Citation (APA)**
Karewar, S., Sietsma, J., & Santofimia Navarro, M. (2018). Effect of pre-existing defects in the parent fcc phase on atomistic mechanisms during the martensitic transformation in pure Fe: A molecular dynamics study. *Acta Materialia*, *142*, 71-81. https://doi.org/10.1016/j.actamat.2017.09.049

Acta Materialia 142 (2018) 71–81

Contents lists available at ScienceDirect

Acta Materialia

journal homepage: www.elsevier.com/locate/actamat

Full length article

# Effect of pre-existing defects in the parent fcc phase on atomistic mechanisms during the martensitic transformation in pure Fe: A molecular dynamics study

S. Karewar*, J. Sietsma, M.J. Santofimia

*Department of Materials Science and Engineering, Delft University of Technology, Mekelweg 2, 2628 CD Delft, The Netherlands*

ARTICLE INFO

*Article history:*
Received 30 June 2017
Received in revised form
14 September 2017
Accepted 21 September 2017
Available online 23 September 2017

*Keywords:*
Martensitic transformations
Twin boundary
Stacking faults
Molecular dynamics
Atomistic mechanisms

ABSTRACT

Molecular dynamics (MD) simulations are used to study the effect of different defect configurations and their arrangements in the parent fcc phase on atomistic mechanisms during the martensitic transformation mechanisms in pure Fe. The defect configurations considered are stacking faults (SF) and twin boundaries (TB) in single crystal fcc. Three arrangements of these defect structures are considered: parallel TB, intersecting SF, and intersecting SF and TB. Each of these defect configurations affect the transformation mechanisms and transformation temperatures. Parallel TB are the lowest-barrier sites for the atomic shear and thus accelerate the transformation process. The fcc phase with parallel TB follows the Nishiyama-Wasserman (NW) martensitic transformation mechanism. On the other hand, intersecting SF impede the atomic shear and thus retard the transformation. The atomistic transformation mechanism in this case first follows the hcp to bcc Burgers path and then the fcc to bcc Olson-Cohen model. The intersecting SF and TB result in a combined effect of both the previous cases. The simulation results show the occurrence of different atomistic mechanisms during martensitic transformation depending on the type of defects present in the parent fcc phase.

## 1. Introduction

The martensitic transformation mechanisms represent a diffusionless type of phase transformation in many material systems such as Zirconia, Titanium, and some Cu alloys. The martensitic transformation involves a coordinated and ordered rearrangement of the atomic configuration [1]. In Fe-C alloys the martensitic transformation represents the change in crystal structure from face-centered-cubic (fcc) austenite to body-centered-cubic (bcc) or body-centered-tetragonal (bct) martensite. This mechanism mainly occurs by the displacive motion of atoms during rapid quenching and plays an important role in the mechanical properties of Fe-C alloys.

The engineering importance of the martensitic transformation has led to significant efforts to explore its transformation mechanisms. Different theoretical models have been proposed in the literature to explain the transformation process, such as Bain model, shear models by Kurdjumov-Sachs (KS) and Nishiyama-Wasserman (NW), a hard sphere model by Bogers-Burgers (BB), and the Olson-Cohen (OC) model which is based on the BB model (BB/OC) [2–7]. Recently a phenomenological theory of martensite transformation (PTMT) and a two step theory by Cayron have been proposed [1,8]. The Bain model considers the lattice expansion in two fcc lattice directions and contraction in the third to achieve the bcc crystal symmetry. The NW and KS models consider atomic shear on alternate $\{111\}$ planes with $[11\bar{2}]$ and $[10\bar{1}]$ fcc directions being invariant, respectively. The BB/OC theory describes the crystal structure change as the nucleation of the bcc phase at the intersection of two stacking faults on two $\{111\}$ planes. The PTMT considers the transformation as a matrix multiplication in two steps: a first step, called invariant plane strain, responsible for the macroscopic shape change and a second step involving shear, to change the crystal structure without shape change. According to PTMT theory the resultant martensite has a twinned structure. The PTMT theory rationalizes the martensitic transformation based on the generation of twinned martensite to accommodate the shape and crystal structure change. The two-step theory considers the atomic displacements by introducing a new parameter called the angle of planar distortion. The details of these models can be found

---

* Corresponding author.
*E-mail address:* karewar1@gmail.com (S. Karewar).

https://doi.org/10.1016/j.actamat.2017.09.049
1359-6454/

in the literature [1,6,7].

The above theories are all based on lattice transformation models and do not take into account the exact atomic displacements during the transformation process, except for the BB/OC model. The BB/OC model considers both the atomic displacements and the transformation process as resulting from the passage of two partial dislocations [8,9]. They also do not consider the effect of pre-existing defects in the parent fcc phase on the martensitic transformation. The different defect structures such as dislocations, stacking faults (SF) and twin boundaries (TB) are important as they are present in the high temperature fcc phase of Fe based alloys depending on the exact alloy composition and the applied heat treatment [1,7,10–12]. Furthermore, in experimental studies it is difficult to separate the effect of each type of defects since more than one defect type will be present at any given temperature in the macroscopic polycrystalline samples. Theoretical models have therefore been difficult to validate and analyse thoroughly at the atomic scale in experiments. The difficulty in analysis also arises from the fact that one or more processes (such as slip, twinning, and shear) can occur simultaneously that are difficult to analyse and correlate. In addition, in-situ observations at the atomic scale are not feasible. Few experimental studies have reported the transformation mechanisms but their results are deduced based on the final microstructure observed [7,11,12]. The details of atomic movements during the transformation process cannot be observed experimentally.

In 1971, Krauss et al. studied the morphology of martensite in various Fe alloys [13]. They concluded that the phenomenological and crystallographic theories of martensitic transformation mainly consider the lattice-invariant deformations. These theories do not consider factors such as the role of austenite and the defects present in the austenite during the shear processes, stacking fault energy of austenite, and the ability of austenite to be stable with respect to the newly forming martensite. Recently, considerations have been given to understand the effect of stacking fault energy changes due to alloying additions on the mechanical properties of steels [14,15]. But other questions are still largely unexplored.

Atomistic simulations methods such as molecular dynamics (MD), have evolved as a powerful tool to analyse the mechanisms which are difficult to observe experimentally. MD simulations have been used to study different aspects in Fe based alloys such as the fcc to bcc transformation at fault intersections by Sinclair et al. [16] and in systems containing bcc/fcc interfaces [17–19]. Wang et al. have studied temperature induced martensitic phase transformations in single crystal Fe-C alloys using MD simulations [20]. They studied the effect of different parameters such as heating and cooling rates on the transformations, and benchmarked these parameters to observe the transformations. They have also discussed the effect of C addition on the transformation temperatures and evolution of stress during transformation. However, they have not discussed the martensitic phase transformation mechanisms in terms of atomistic processes.

The present MD study aims to observe the precise atomic displacements associated with the fcc to bcc transformation during thermal quenching in presence of pre-existing defects in the parent fcc phase. We aim to answer some of the above questions, related to the role of austenite and the defects inside it on the martensitic transformations, on the basis of the MD simulations on pure Fe. In particular we focus on the atomic shear that takes place in the parent fcc austenite phase in presence of defects and the role of austenite transforming to martensite. The defect structures considered here are planar defects such as SF and TB in the parent fcc phase.

The paper is organized as follows. In Section 2, we introduce the simulation methodology and defect structures in the parent fcc phase developed during heating. In Section 3, we will discuss the phase transformation mechanisms from fcc to bcc during cooling. Section 4 describes and discusses the effect of defect structures on the transformation mechanisms and transformation temperatures.

## 2. Simulation methodology

The choice of interatomic potential is most critical for MD studies. We have used the Meyer-Entel embedded atom method potential for the simulations in the present work [21]. Engin et al. [22] characterized six different embedded atom method (EAM) type potentials in the literature to conclude that only the Meyer-Entel potential can describe both the bcc-to-fcc and fcc-to-bcc transformation. The Meyer-Entel potential has been used in the literature previously to study the fcc and bcc phases in pure Fe [20,23–25]. The limitations of this EAM type potential is that it does not consider the magnetic effects which play an important role in the thermodynamic and equilibrium properties of Fe. Although this influences the relative stability of the two phases, the transformation mechanisms can be assumed not to be influenced by this shortcoming [26]. This potential predicts that the atomic volume of fcc is greater than bcc, since the lattice constant of fcc phase for this potential is 3.686 Å whereas experimentally it is found to be 3.571 Å [27]. The implication of the slightly higher atomic volume is that a volume increase is observed during bcc-to-fcc transformation and a decrease is observed during fcc-to-bcc transformation, which is opposite to what is observed experimentally. Song et al. studied the nucleation kinetics of the bcc phase at the grain boundaries of fcc nano-polycrystalline Fe with a potential which shows the opposite trend for the fcc-bcc volume change and found that this discrepancy does not affect the nucleation and growth of the bcc phase at the fcc grain boundaries [28]. In addition, we also calculated the stacking fault energy (SFE) of the fcc phase of Meyer-Entel potential along the $\{111\} < 112 >$ slip system. The SFE value is -54 mJ/m$^2$. Two recent first principles studies on the fcc Fe mention that the SFE value of non-magnetic fcc Fe is -415 mJ/m$^2$, whereas for paramagnetic fcc Fe it is -105 mJ/m$^2$ [29,30]. Therefore, we can conclude that the SFE of the Meyer-Entel potential is in much better agreement with the paramagnetic fcc phase even though the EAM formalism of the potential does not consider the magnetism explicitly. The important thing to note here is that the magnitude of the SFE is negative both from the Meyer-Entel potential and first principles data, which indicates a spontaneous formation of the planar defects in the fcc phase. The SFE of the modified embedded atom method (MEAM) type potential by Lee et al. for the fcc phase was found to be positive (+37.5 mJ/m$^2$) in opposite trend to the first principles data [31,32], therefore we do not use this potential. For the present work, it is very important to have the correct energetics of the planar defects, in this case SF, with respect to the first principles data; because it is this energetics that controls the stability of the planar defects in the fcc phase. The presence of stable planar defects will in turn have an effect on the atomistic transformation pathways. Considering these arguments, literature studies, and the matching of the SFE value with the first principles data, we use the Meyer-Entel potential in the present work to analyse the effect of planar defects on the fcc-to-bcc transformation process.

The supercell used for pure Fe as the starting point of the simulations is a single crystal bcc system with periodic boundaries in all three directions. The supercell sizes used are 15*15*15 and 20*20*20 unit cells in X, Y, and Z directions, respectively. NPT ensemble is used to control the temperature and pressure of the simulation system. First the energy minimization of the supercell is done at 0 K to obtain the correct lattice constants and energy of the system. The system is then equilibrated at 50 K for 100 ps so that the pressure is reduced to less than 5 MPa. The system is heated from 50 K to 1600 K at 1 K/ps. During heating the crystal structure changes from bcc-to-fcc at 1300 K. During simulations with different initial velocities, fcc phase attained three different arrangements of the defects at 1300 K which will be discussed below in detail. The bcc-to-fcc transformation during heating has been discussed in the literature for Fe alloys by MD simulations [20,27,33,34]. The fcc structure is then cooled from 1600 K to 50 K. The cooling rate used is 1 K/ps. The effect of different parameters of simulations such as heating and cooling rates, and evolution of pressure during simulations has been discussed in the literature in detail [20]. We will focus on the martensitic phase transition mechanisms when the system transforms from fcc to bcc in this work. LAMMPS MD code is used for the simulations [35]. Visualization software OVITO is used to visualize and analyse the microstructure of the simulation system [36]. The crystal structure is identified by the adaptive common neighbour analysis (a-CNA) method and atomic displacements are calculated by using the displacement calculation modifier, both of which are implemented in the OVITO software. The atomic displacements are scaled by a factor of three in the figures for better visibility.

Before exploring the microstructure of the simulation systems, we will first characterize the signatures of defects in the fcc austenite phase. The defects in consideration, SF and TB, are planar defects and formed by the interruption in the perfect stacking sequence of the fcc atomic layers [37]. For the perfect fcc crystal structure, the stacking sequence of closed packed planes along [111] direction is “ABCABC …” as shown in Fig. 1(a). The SF in the fcc phase have the local symmetry, “BAB”, of the hcp phase. The a-CNA method identifies the SF as two atomic layers of hcp phase shown in red in Fig. 1(b). The atomic layer stacking above and below SF is the same. The TB are identified as single layer of hcp atoms by the a-CNA analysis method as shown by the single red atomic layer in Fig. 1(c). For the TB labelled as the atomic layer “B” in this figure, the perfect fcc stacking above and below it are mirror images of each other. The solid black lines also indicate the mirror image {111} planes across the TB.

The bcc → fcc transformation during heating produces three different defect configurations of twin boundaries (TB) and stacking faults (SF) inside the parent fcc phase at 1300 K. They are:

(i) TB which are parallel to each other,
(ii) SF which intersect each other, and
(iii) TB and SF which intersect each other.

Fig. 2(a) shows the relative volume, $\frac{V}{V_0}$, vs temperature during cooling from 1600 K for three fcc crystals with the above three defect configurations. Here $V_0$ is the volume of the single crystal bcc simulation system at 50 K after 100 ps equilibration. The sudden decrease in volume during cooling indicates the transformation from fcc to bcc phase. The respective transformation temperatures are marked in this figure for different defect types. For fcc phase with parallel TB the transformation starts at 300 K, for intersecting SF it starts at 180 K, and for intersecting SF and TB it starts at 290 K.

These three defect structures are formed in the fcc phase from three different initial velocity trajectories of bcc phase during heating and are shown in Fig. 2(b–d). The spontaneous formation of these defect structures in the fcc phase can be explained based on the value of the SFE which is negative, as mentioned above, for the Meyer-Entel potential used in this work. The negative magnitude of the SFE of the Meyer-Entel potential is consistent with the first principles studies of fcc Fe [29,30]. The negative value indicates stable planar defects in the fcc phase. These stable planar defects form in the fcc phase to relieve the high internal atomic stresses which would be generated in an otherwise perfect fcc single crystal without any defects. The observation of these defects is not entirely unexpected. In fact, they are observed in fcc austenite phase in various experiments as well [1,10]. The three configurations shown in Fig. 2(b–d) are the starting simulation systems to study the transformation mechanisms from fcc to bcc upon cooling. The defect structure inside the fcc phase affects the transformation mechanism to bcc phase during cooling. These mechanisms are discussed in the next section.

With Meyer-Entel potential, the perfect single crystal fcc phase with no defects inside it is not stable below 500 K with respect to bcc phase. However, for kinetic reasons it does not transform to bcc phase. Although the $\Delta G_{(fcc-bcc)} < 0$ for the Meyer-Entel potential at temperatures below 500 K [22], the transformation barrier for the fcc to bcc phase can be high and therefore the fcc is meta-stable at the temperatures studied here. Indeed, it has been shown by Sandoval et al. using nudged elastic band method that stresses as high as upto 2 GPa are observed during fcc-to-bcc transformation which follows the NW path [25]. This indicates that the pressure can induce fcc-to-bcc transformation in a single crystal fcc phase

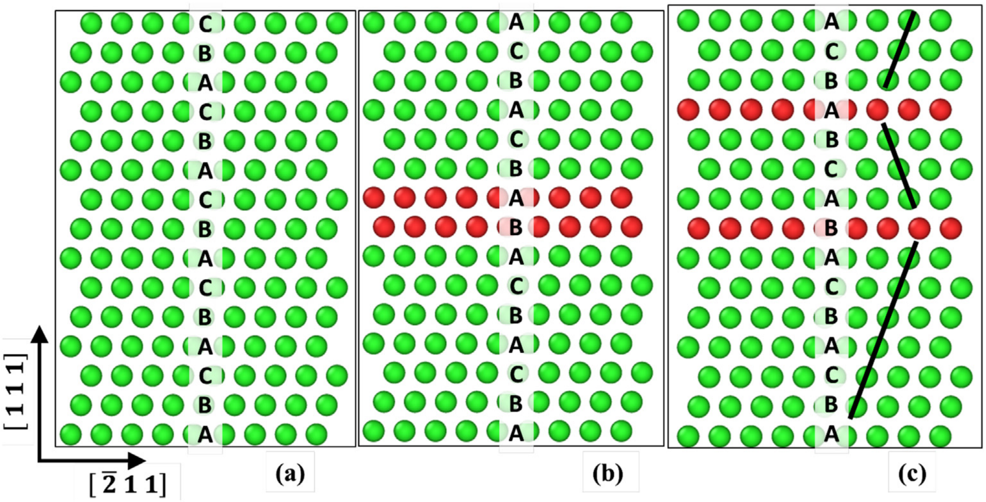

Fig. 1. The stacking sequence of the closest packed planes for the (a) perfect fcc crystal structure (b) stacking fault in the fcc phase (c) 4-layer twin in fcc phase. Atoms are coloured as per a-CNA: green-fcc, blue-bcc, red-hcp. (For interpretation of the references to colour in this figure legend, the reader is referred to the web version of this article.)

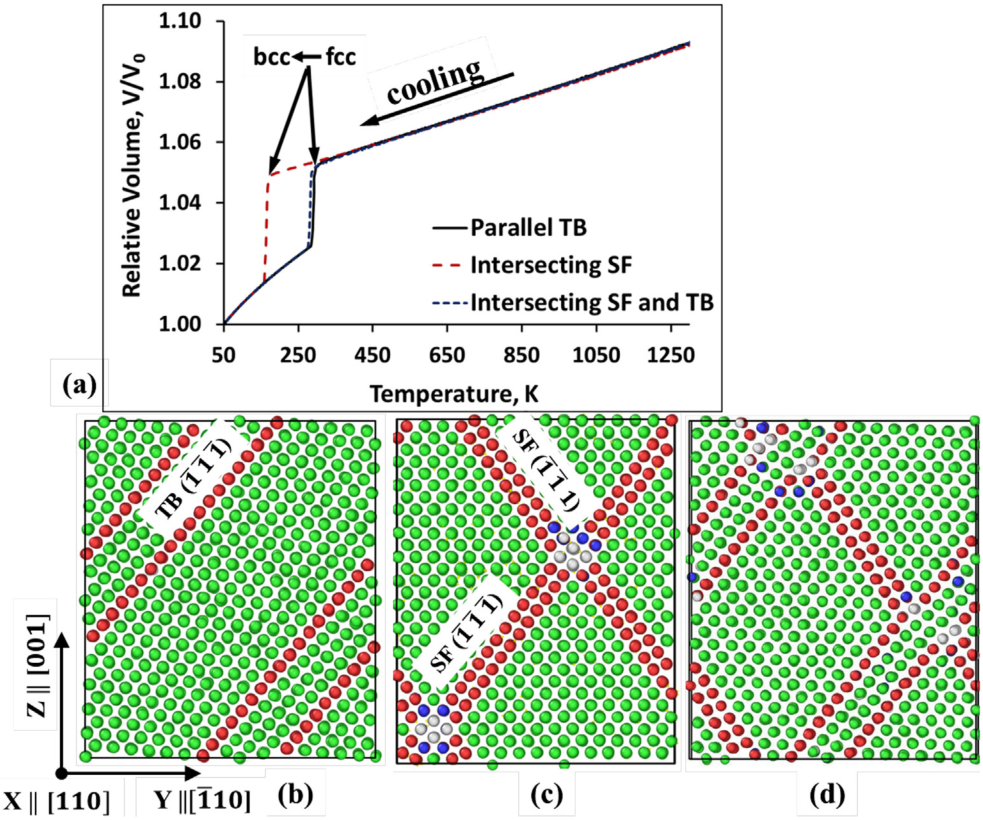

**Fig. 2.** (a) Volume vs temperature curve during cooling for pure Fe with different defect structures in the fcc austenite phase. The three different defect structures formed in the fcc phase of Pure Fe at 1300 K (b) parallel TB, (c) Intersecting SF, and (d) Intersecting SF and TB. Atoms are coloured as per a-CNA: green-fcc, blue-bcc, red-hcp, and grey-unidentified. (For interpretation of the references to colour in this figure legend, the reader is referred to the web version of this article.)

without any defects using Meyer-Entel potential. But the pressure induced transformation and the atomistic pathway followed during it is beyond the scope of the present work, in which we aim to analyse the temperature induced fcc-to-bcc transformation in presence of the planar defects, and can be a part of the separate research. In the view of the lack of MD simulations, alternatively, the transformation mechanism of the ideal fcc single crystal can be referenced to or derived from the available literature models such as NW or KS. Therefore we have compared our results with these lattice translation models.

## 3. Results

### 3.1. Transformation during cooling from fcc to bcc: the case of parallel TB inside the parent fcc phase

Fig. 3 shows the microstructure evolution as a function of decrease in temperature for the fcc phase with parallel TB. At 350 K, the TB in the fcc phase are seen as single layers of atoms in hcp on the $(\bar{1}\bar{1}1)$ plane, represented in red in Fig. 3(a). For clarity, we will discuss the atomic configuration change during the fcc to bcc transformation in the marked rectangular area in Fig. 3(a), which is a representative area for the entire simulation cell and captures all the atomic features under consideration i.e. fcc phase and TB.

At 300 K, atoms of the two TB start to shear on the $(\bar{1}\bar{1}1)$ fcc plane along the two opposite $[11\bar{2}]$ type directions. This shear is represented by the atomic displacements of the atoms with respect to original fcc atom positions, shown by black arrows in Fig. 3(b). The position of the TB in the original fcc phase is shown by the red triangles. This shear displacement of the TB changes the crystal structure from fcc to bcc.

With further decrease in temperature, the fcc atom layers parallel to TB start to shear on the $(\bar{1}\bar{1}1)$ plane. The pronounced displacement on the parallel layers is seen in Fig. 3(c), shown by black arrows, which transforms the fcc phase to bcc crystal structure. This shear of the TB and atomic layers parallel to it completes the transformation to bcc phase at 280 K. The atomic layers next to TB assume the same shear direction as that of the closest TB. The $(\bar{1}\bar{1}1)$ atomic layer in between the two TB do not undergo shear displacements when the structure is transforming to bcc phase. This atomic layer with no shear displacement is shown by the yellow triangle in Fig. 3(c). This layer of atoms on the $(\bar{1}\bar{1}1)[11\bar{2}]_{fcc}$ slip system is invariant during the transformation and changes to $(011)\left[01\bar{1}\right]_{bcc}$ after the transformation. Therefore the relationship between the fcc and bcc phase during the transformation can be written as

$$\left(\bar{1}\bar{1}1\right)_{fcc}\Big|\Big|(011)_{bcc},\ \left[11\bar{2}\right]_{fcc}\Big|\Big|\left[01\bar{1}\right]_{bcc}$$

This shear mechanism of the fcc to bcc transformation is conceptually similar to Nishiyama-Wasserman (NW) mechanism [1,3,4]. In the 1930's Nishiyama and Wasserman separately postulated that the change in crystal structure from fcc-to-bcc takes place by the shear of fcc atoms on alternate $\{111\}$ planes along the two opposite $\langle 112\rangle$ directions, which is followed by the expansion/contraction of the lattice to achieve the correct atomic density. The $[11\bar{2}]$ direction on the $(\bar{1}\bar{1}1)$ plane in between the two shearing planes is the invariant direction during the transformation. This

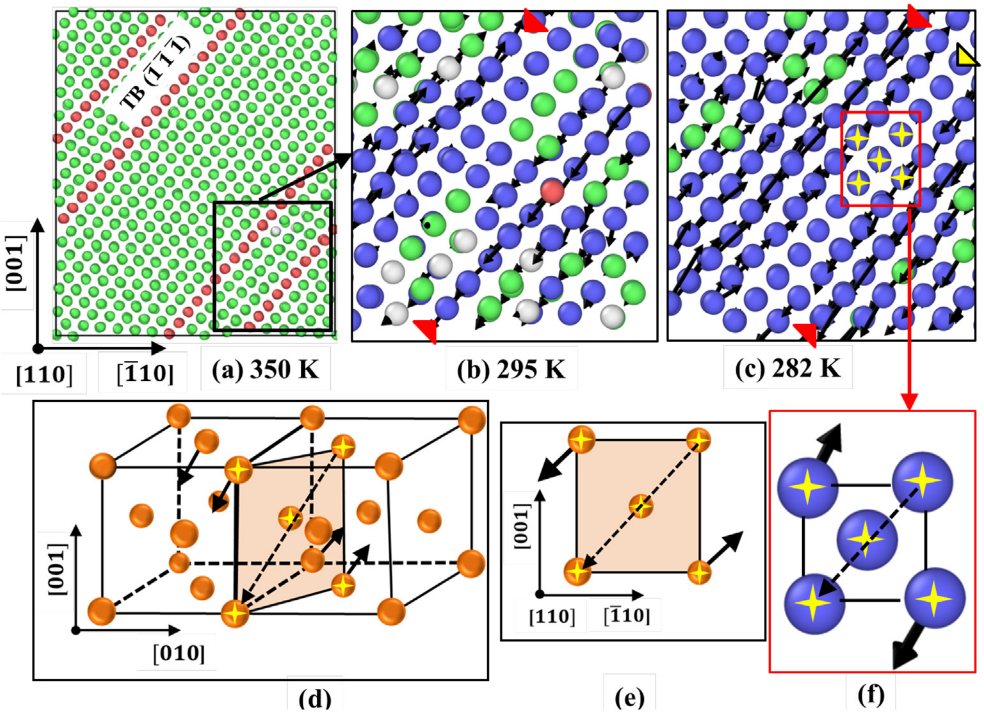

**Fig. 3.** Change in crystal structure from fcc to bcc with decrease in temperature for the case of fcc phase with parallel TB. Atom colours in (a-c,f) are the same as in Fig. 2. The solid black arrows represent the atomic displacements scaled by a factor of three for better visibility. (a) At 350 K, (b) 295 K, and (c) 282 K. (d–e) The NW mechanism schematic along two different projections is shown [25], (f) Atomic displacements from the MD simulations corresponding to the NW mechanism projection in (e). (For interpretation of the references to colour in this figure legend, the reader is referred to the web version of this article.)

mechanism is schematically shown in Fig. 3(d) and in Fig. 3(e) in projection on the (110) plane. Two unit cells of fcc crystal structure are shown by the orange atoms and the atoms marked with yellow stars indicate the bcc unit cell configuration inside the two fcc unit cells. The solid black arrows indicate the direction of the shear of the atoms and the dashed arrow shows the invariant direction. The plane shown in orange is visible in the [110] direction projection as seen in Fig. 3(e). Fig. 3(f) shows the five atoms in bcc phase from MD simulations and their atomic displacements with respect to the original fcc phase. In this figure, the change in crystal structure from fcc to bcc due to the atomic displacements and the invariant line during this change are the same as shown in the schematic Fig. 3(e). The opposite directions of the atomic displacements in Fig. 3(e–f) indicate the opposite $<112>$ directions. This matching confirms the occurrence of the NW mechanism for the change in crystal structure from fcc with parallel TB to bcc.

Fig. 4 shows a different view of the NW transformation mechanism and the MD microstructural evolution [3]. In this mechanism, the parallelepiped fcc unit cell with 70°32′ angle (green atoms with stars) between the two fcc lattice directions, [112] and $[11\bar{2}]$ , changes to a bcc unit cell with a 90° angle (blue atoms with stars), between the bcc directions [011] and $[01\bar{1}]$, as shown in Fig. 4(d). This $19^0 28'$ shear causes the change from fcc-to-bcc. Fig. 4(a–c) show the fcc-to-bcc transformation with decrease in temperature from the MD simulations. We selected three atoms along the same lattice directions in Fig. 4(b–c) as in Fig. 4(d) and tracked their angle and displacements. The close up view of these three atoms is shown in Fig. 4(e–f). It can be seen that these fcc atoms have 70°32′ angle at 350 K and the atomic shear with the decrease in temperature to 280 K changes this angle to $90^0$. These atoms thus assume the bcc configuration. This $19^0 28'$ shear changes the structure to bcc.

In summary, the simulations show that the fcc phase with parallel TB changes to bcc by the shear of atoms on two {111} planes in two opposite ⟨112⟩ directions. The shear displacements start at the TB plane and then the atomic layers parallel to TB start shearing on {111} planes. No displacement is observed in the atomic layer between the two TB and thus it is the invariant plane during this change in crystal structure. This mechanism is the same as the NW transformation mechanism.

### *3.2. Transformation during cooling from fcc-to-bcc: the case of intersecting SF inside the parent fcc phase*

Figs. 5 and 6 show the change in crystal structure from fcc phase with intersecting SF to bcc phase. The fcc-to-bcc configuration change in this case is a combination of two steps. The first step is shown in Fig. 5. At 200 K, the fcc phase has two SF intersecting on two {111} planes, shown in Fig. 5(a). The changes in the marked rectangular area in this figure are shown and discussed. The atoms of one of the atomic layers of the SF, which locally have the hcp structure, start shearing on the $(1\bar{1}00)[11\bar{2}0]$ slip system at 190 K and the increased magnitude of the displacements, shown by solid black arrows, changes the symmetry to bcc at 170 K, seen in Fig. 5(b–c). At 170 K, only the SF atoms in the simulation system change to bcc, as seen in 5(d). The position of the original SF in this figure is marked by red triangles. This mechanism of transformation is the same as the hcp to bcc Burgers path. In 1930 Burgers studied the bcc ↔ hcp transformation in Zr and postulated that the $\{0001\}_{hcp}$ plane change to $\{110\}_{bcc}$ plane by the shear of the atoms on the prismatic plane $(1\bar{1}00)_{hcp}$ along the $\langle 11\bar{2}0 \rangle$ direction. This mechanism is shown schematically in Fig. 5(e) [1]. The two atomic layers of $\{0001\}_{hcp}$ plane are shown: open circles are on the top plane and filled circles are atoms of the bottom plane. This

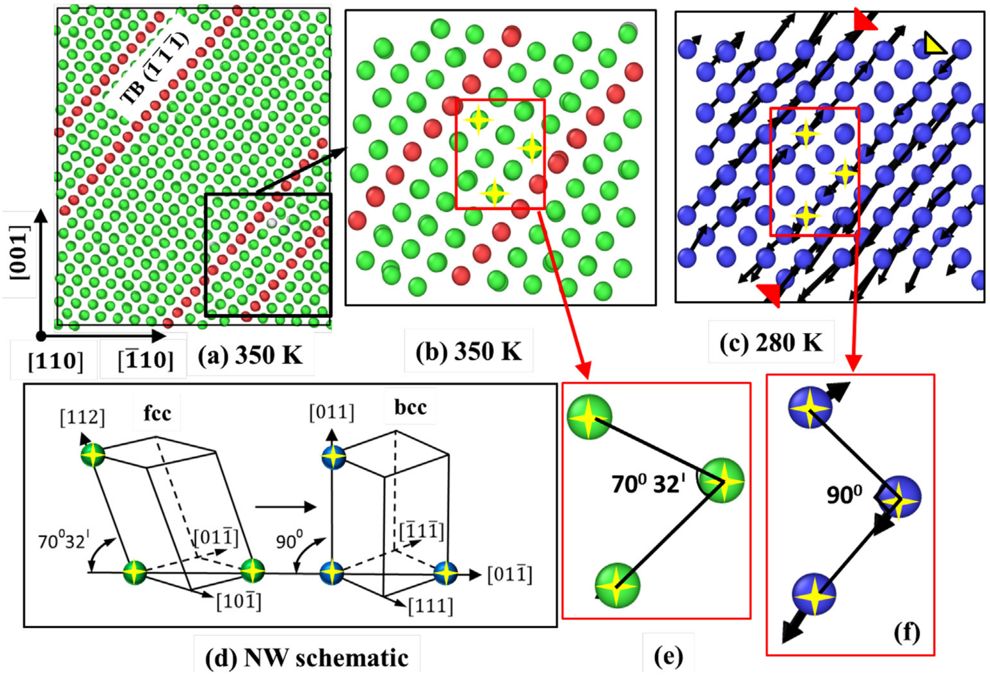

**Fig. 4.** Change in crystal structure from fcc-to-bcc with decrease in temperature for the case of fcc phase with parallel TB. Atom colours are the same as in Fig. 2. The solid black arrows represent the atomic displacements scaled by a factor of three for better visibility. (a) 350 K, (b) 350 K, and (c) 280 K (d) NW schematic relation in a different perspective is shown [1], (e–f) change in crystal structure according to the NW schematic. (For interpretation of the references to colour in this figure legend, the reader is referred to the web version of this article.)

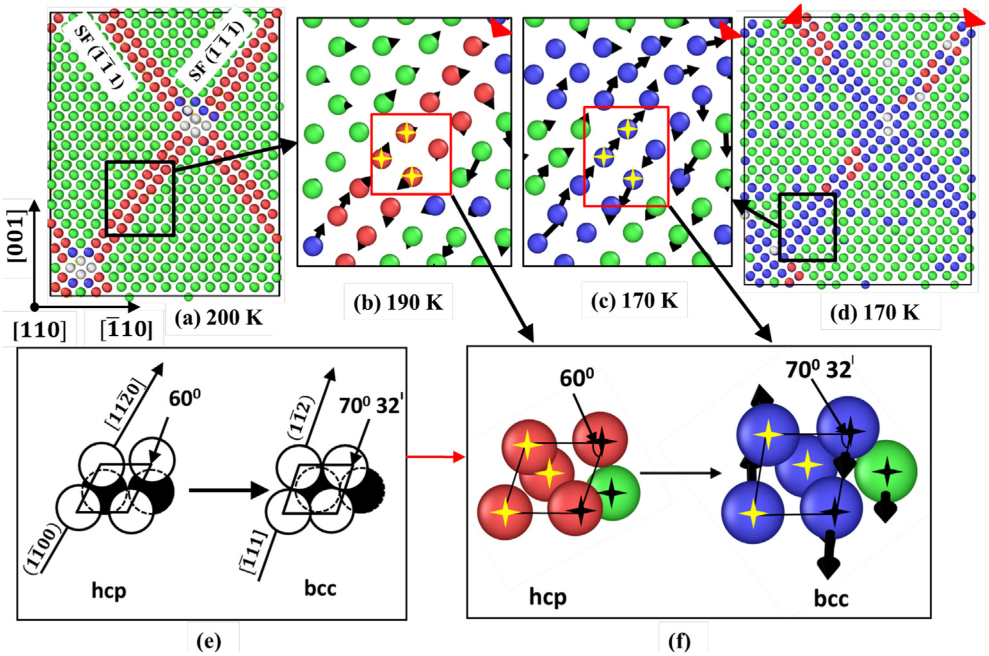

**Fig. 5.** Microstructural evolution with decrease in temperature for the fcc phase with intersecting SF. Atom colours are the same as in Fig. 2. The solid black arrows represent the atomic displacements scaled by a factor of three for better visibility. (a) 200 K, (b) 190 K, (c–d) 170 K, (e) hcp to bcc Burgers transformation path is shown schematically [1]. (f) The corresponding transformation of six atoms in the SF plane according to the schematic. These atoms are marked by yellow stars in (b–c) respectively. Atoms with black stars are the extra atoms visible in different projection. (For interpretation of the references to colour in this figure legend, the reader is referred to the web version of this article.)

shear changes the angles on the respective planes from 60° in hcp to $72^0 32'$ in bcc. We tracked and projected six atoms from the present MD simulations along the same projection as in Fig. 5(e) and found the same shear direction and change in angle as for the Burgers path. The corresponding MD simulation results are shown in Fig. 5(f). The projection direction of the atoms is different in Fig. 5(a–d) and 5(e-f) as indicated in Fig. 5(a) and (e), respectively. In Fig. 5(f), atoms marked with yellow stars represent the same atoms as in Fig. 5(b–c) and atoms marked by black stars represent the extra atoms in the hcp symmetry visible in different projection.

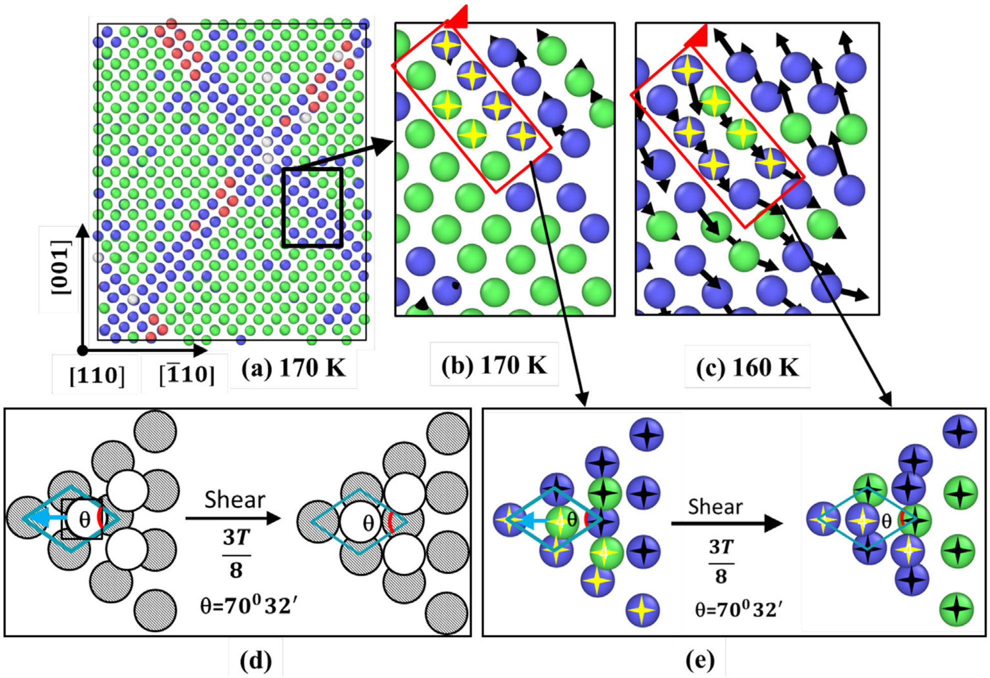

**Fig. 6.** Change in crystal structure with decrease in temperature for fcc phase with intersecting SF. Atom colours are the same as in Fig. 2. The solid black arrows represent the atomic displacements scaled by a factor of three for better visibility. (a) The atomic configuration after hcp to bcc transformation is shown at 170 K. Magnified view in the marked rectangular area is shown in (b) at 170 K and (c) at 160 K, (d) BB/OC transformation model schematic [6,7]. (e) The shearing of the MD simulation atoms as per the BB/OC transformation schematic. $T = \frac{a}{6}\langle 112\rangle$ is the Burgers vector of the Shockley partial for the fcc twin shear. The atoms marked by yellow stars are from figure (b–c) respectively. Atoms with black stars are the extra atoms visible in different projection. (For interpretation of the references to colour in this figure legend, the reader is referred to the web version of this article.)

Once the atoms of the SF have changed the crystal structure from hcp to bcc, the shear in the rest of the fcc phase takes place. Fig. 6 shows the simulation system at 170 K where the atoms of the SF have changed from hcp to bcc. Fig. 6(b–c) shows a close up view of the simulation system with decrease in temperature. The fcc atomic layers which are parallel to the transformed bcc atomic layer or to the original SF, start shearing on the $\{111\} < 112 >$ slip system. This shearing changes the crystal structure from fcc-to-bcc. The transformation of the atomic layers of fcc phase because of the shearing is shown schematically on the $\{111\}_{fcc}$ plane from the literature [6,7] and from the present MD simulations in Fig. 6(d) and (e), respectively.

The BB/OC model is based on the Bogers-Burgers hard-sphere model, further developed by Olson-Cohen in 1972 [6,7]. According to this mechanism, the shearing and intersection of the two SF on two different $\{111\}$ planes of fcc phase nucleates the bcc phase at the intersection. The two shears in this model are "$\frac{T}{3}$" and "$\frac{3T}{8}$", where $T = \frac{a}{6}\langle 112\rangle$ is the Burgers vector of the Shockley partial for the fcc twin shear. Fig. 6(d) shows the configuration of the $(110)_{bcc}$ plane after the first shear $\frac{T}{3}$ on the left side and the configuration after the second shear on the right side. The open circles denote the atoms on the top layer and filled circles are the atoms on the bottom layer. We tracked the motion of the atoms in the present simulations shown in Fig. 6(e). The projection direction of the atoms is different in Fig. 6(a–c) and 6(d-e). In Fig. 6(e), atoms marked with yellow stars represent the same atoms as in Fig. 6(b–c) and atoms marked by black stars represent the extra atoms visible in different projection. The configuration on the left side in Fig. 6(e) is a $\{111\}$ plane after first shear $\frac{T}{3}$. The bottom atoms are in the bcc phase (blue) and top layer atoms have fcc symmetry (green). The second shear $\frac{3T}{8}$ changes the atomic configuration to bcc phase as seen from the configuration on the right side of Fig. 6(e). This shear from the MD simulations is the same as the second shear of the BB/OC model seen in Fig. 6(d–e).

Thus the transformation for the fcc phase with intersecting SF is a combination of hcp to bcc Burgers path for the SF atoms and the BB/OC model for the fcc atoms.

### *3.3. Transformation during cooling from fcc-to-bcc: the case of intersecting TB and SF inside the parent fcc phase*

Fig. 7 shows the transformation from fcc phase with intersecting SF and TB. The transformation mechanism in this case is a combination of mechanisms discussed in the previous two cases. Fig. 7(a) shows the fcc phase with intersecting TB and SF at 300 K. The magnified view of the transformation mechanisms of SF and TB atoms are shown in Fig. 7(b–d) for the marked rectangular areas. Fig. 7(b–d) shows a single layer of atoms for better visibility. The atomic displacements are shown in black arrows with respect to the positions of the original fcc crystal positions. The red triangles show the position of the TB or SF in the original fcc phase before transformation.

The shear displacements start at the TB which is followed by the atomic shears at the SF layers. The configuration of the atoms of the TB changes to bcc crystal structure by NW mechanism of the shearing on alternate $\{111\}$ plane in two opposite $< 112 >$ directions, seen in Fig. 7(b). The opposite displacements are shown by black arrows on the TB plane indicated by the red triangle. The atoms at the SF configuration shear according to the Burgers path to change the structure from hcp to bcc, seen in Fig. 7(c). Once the transformation at TB and SF is completed, the atoms in the rest of the fcc phase in the simulation system start to shear. The atoms with fcc structure near TB follow the NW mechanism and displace in the same direction as the nearest TB. The fcc atoms closer to SF follow the second shear of the BB/OC model to transform to the bcc

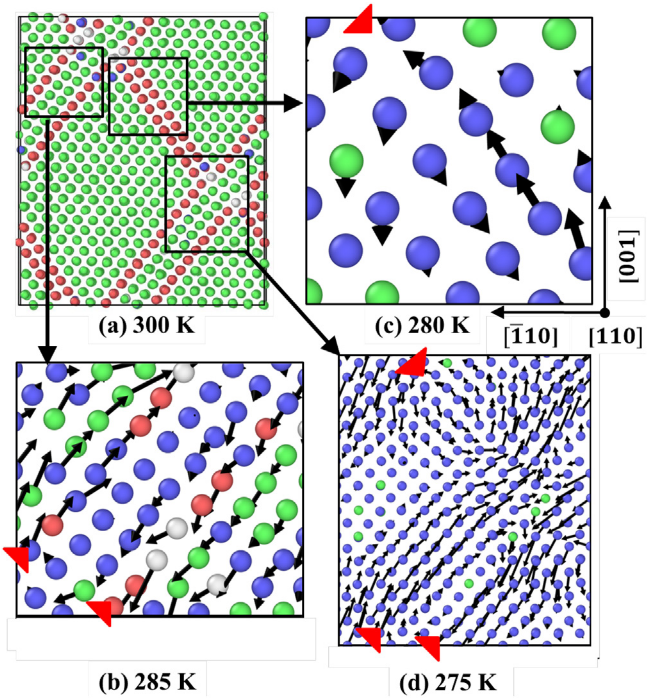

**Fig. 7.** The change in crystal structure for fcc phase with intersecting SF and TB. Atom colours are the same as in Fig. 2. The solid black arrows represent the atomic displacements scaled by a factor of three for better visibility. (a) 300 K, (b) 285 K, (c) 280 K, (d) 275 K. (For interpretation of the references to colour in this figure legend, the reader is referred to the web version of this article.)

phase. At 275 K, the transformation is completed when all atomic layers parallel to SF and TB also shear, as shown in Fig. 7(d). Fig. 7(d) shows a close-up view at the intersection of TB and SF. It can be seen that in this region both mechanisms, NW and Burgers, are active. The change in crystal structure in this case is therefore a combination of the two previous cases.

## 4. Discussion

In the previous section, we discussed that the different defect structures affect the atomistic transformation mechanisms and the transformation temperatures from fcc-to-bcc phase. The defect structures aid the cooperative and ordered rearrangement of the atoms during the martensitic transformation. Diffusional motion of the atoms is not observed in the present simulations. The fcc phase with parallel TB transforms by NW mechanisms, whereas the fcc phase with intersecting SF transforms by a combination of Burgers path and BB/OC model. The fcc phase with intersecting SF and TB follows both the previous mechanisms. It is interesting to note that although the NW and BB/OC are based on lattice translation models, both are applicable to the atomic shear observed in the present simulations depending on the defects present in the fcc phase.

In order to understand how the defect configurations affect the change in crystal structure from fcc-to-bcc, we calculate and analyse the resolved atomic shear stress $\tau_r$ on the slip system $\{111\} < 112 >$ in fcc phase at 400 K. It is calculated by

$$\tau_r = m * S_{zz} \tag{1}$$

where $m$ is the Schmid factor, and $S_{zz}$ are the atomic stresses along the Z || [001] direction of the simulation system shown in Fig. 1. The stresses along the Z direction, $S_{zz}$, are resolved along the atomic shear direction to qualitatively analyse the stress states that affect the atomic displacements. These atomic stresses are indicated in Fig. 8(a–c) for the three configurations with defect structures in the MD simulations. Positive stresses indicate tensile stress state and negative stresses indicate compressive stress state. Red triangles again indicate the positions of TB and SF in the original fcc phase.

For fcc phase with parallel TB, as seen in Fig. 8(a), two distinct regions of stress states are observed across the TB atomic layers. These two regions are separated by dotted lines in this figure. The compressive stress and tensile stress states are seen to be alternating across the TB, whereas the atoms of the TB have both the tensile and compressive stress states and therefore the average stress on the atoms of the TB is closer to 0. We calculated the average stress on the TB atomic layer in the fcc phase and found it to be $-0.02 \pm 0.01$ GPa. The average stresses in the tensile and compressive regions are $0.2 \pm 0.1$ GPa and $-0.2 \pm 0.1$ GPa, respectively. The atoms of the TB experience lowest shear stresses, but still initiate the transformation. They therefore require lowest magnitude of the shear stress for the displacements. Thus the local atomic configuration around TB acts as a low barrier site for the atomic displacements. The shear displacements of the atoms, which locally start at the TB, are shown in Figs. 3(b) and 7(b). The atomic layers closer to the TB then follow the same shear direction of the TB seen in Figs. 3(c) and 7(b). Thus for the fcc phase with parallel TB the shear displacements start at the TB because of the lowest magnitude of the barrier i.e. atomic shear stresses needed for the displacement.

For fcc phase with intersecting SF, seen in Fig. 8(b), the two SF intersect on the two $\{111\}$ planes to form a Lomer-Cottrel (LC) lock according to the following reaction of the Burgers vectors:

$$\frac{a}{6}\left[\bar{1}21\right] + \frac{a}{6}\left[2\bar{1}\bar{1}\right] = \frac{a}{6}[110] \tag{2}$$

The LC lock is sessile in nature and therefore creates a barrier for the motion of the atoms. The four layers of the atoms of the LC are shown by solid circle in Fig. 8(b) for easy identification and can also be seen as unidentified atoms in Fig. 5(a). The sessile nature of LC atoms creates high atomic shear stresses at the intersection until the barrier for the atomic shear is crossed with decrease in temperature. The rest of the fcc has average stresses closer to zero. The high atomic stress regions of SF are also shown between the dashed lines in Fig. 8(b).

The two layers of SF have maximum and opposite resolved shear stresses, $\tau_r$, at the intersection. The positive and negative shear stresses on the two layers of the SF indicate the tensile and compressive stresses, respectively. The opposite nature of $\tau_r$ imparts opposite shear on the two atomic layers of SF surface and is responsible for hcp-to-bcc phase transition as seen in the previous section. The stresses are concentrated at the intersection which causes it to serve as a barrier for the atomic displacement.

In the present MD simulations the nucleation of the bcc crystal structure is not observed at the intersection of two SF. Instead these atoms have an unidentified crystal symmetry shown in grey in Fig. 5(a). The nucleation of bcc phase at intersection bands such as dislocations, stacking faults, shear bands, or ε-hcp phase, is referred to as the strain-induced martensite nucleation in the literature [6,7,38]. The partial dislocations intersection is prominent for the Fe alloys with low stacking fault energy (SFE) for fcc austenite phase. It is postulated that high stress concentrations may develop at the intersecting regions of the partial dislocations to induce the nucleation process of $\alpha'$-martensite phase. The intersection of SF can alternatively lead to the formation of sessile LC locks, which is a competing mechanism for the $\alpha'$-martensite nucleation [6,7,38]. The LC lock is considered to be opposing martensite nucleation by

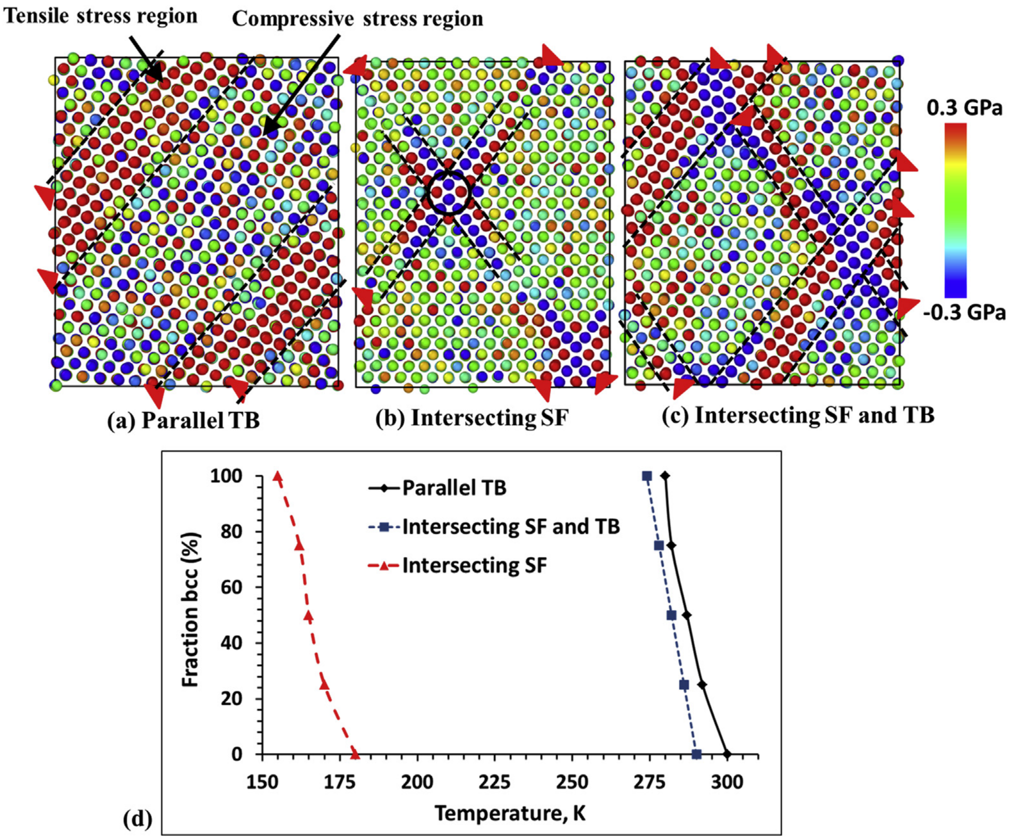

**Fig. 8.** The resolved atomic shear stress, $\tau_r$, on $\{111\} < 112 >$ slip system for Pure Fe at 400 K. Atoms are colour coded as per the $\tau_r$. (a) fcc phase with parallel TB and (b) fcc phase with intersecting SF, (c) fcc phase with intersecting SF and TB, (d) Fraction of bcc phase as a function of temperature. (For interpretation of the references to colour in this figure legend, the reader is referred to the web version of this article.)

shear mechanism as it impedes the further displacement of the atoms.

The present MD simulations show that the intersection of two SF forms LC locks but this does not obstruct the change in crystal structure from fcc-to-bcc. The LC lock is sessile in nature and high stress concentrations are observed at the intersecting region of two SF, as seen in Fig. 8(b). The high atomic stresses piled up at the intersection lead to the shear of the two atomic layers of the SF and the transformation from hcp to bcc takes place by the Burgers path. Thus here we observe an alternative shear mechanism, i.e. Burgers path, for the transformation from fcc austenite with hcp SF defects in the fcc phase.

The fcc phase with intersecting SF represents a higher barrier for the transformation compared to the fcc phase with parallel TB. The atomic stresses are piled-up at the sessile LC lock until the shear of the two SF atomic layers in opposite direction starts the transformation from hcp-to-bcc. This atomic shear requires a greater thermal undercooling. Thus the fcc phase with intersecting SF changes the crystal structure to bcc at a lower temperature than fcc phase with parallel TB.

For the fcc phase with intersecting SF and TB, the stress state is a combination of the two previous cases, as shown in Fig. 8(c). The tensile and compressive stress regions are alternating across the TB, and at the intersection of SF and TB the two atomic layers of SF have high atomic stresses which are equal and opposite in magnitude.

The fraction of bcc phase for three defect structures vs transformation temperature is shown in Fig. 8(d). The fcc phase with parallel TB changes the crystal structure to bcc at a high temperature compared to the other two simulation systems. The transformation starts at 300 K and finishes at 280 K with all the atoms being in bcc crystal structure. The atoms of the TB displace at low shear stresses and thus it is relatively easy for this system to change the crystal structure. The fcc phase with intersecting SF needs greater undercooling or lower transformation temperature to cross the barrier formed by the sessile LC locks. The change in crystal structure starts at 180 K in this case and finishes at 155 K. The transformation start temperature is lower by 120 K for intersecting SF than for the parallel TB, and this is because of the difference in the barriers for the atomic shear. For the third case, intersecting SF and TB, the transformation starts at 290 K and finishes at 274 K. The transformation start temperature is lower than the fcc phase with parallel TB by 10 K and higher than intersecting SF by 110 K. The temperature at the start of the transformation in this system, which is in between the other two cases, indicates that both defect types play a role in the transformation, with TB playing the dominant role in the atomic shears. The dominance of the TB is also indicated by the fact that atomic displacements first start at the TB, as seen in Fig. 7(b) and at the higher transformation temperature as seen in Fig. 8(d).

Thus this section discusses the effect of the different defect structures on the transformation mechanisms and transformation temperatures. Each of the defect structure generates a different atomic arrangement, each of which has a different barrier for the atomic shear. Depending on the barrier for the atomic shear for fcc phase with a particular defect configuration, different degree of under-cooling is needed to change the crystal structure from fcc to bcc. The simulations show that more than one type of martensitic transformation mechanism can take place during the fcc-to-bcc crystal structure change depending on the type of the defects present in the parent fcc austenite phase. It is worthwhile to note that these planar defects are always present in the parent fcc austenite phase of the Fe depending on the exact alloying composition and the heat treatment or mechanical treatment carried out. The current theories on the martensitic transformations are based on the lattice transformation models in single crystals. They do not consider two issues- first the effect of pre-existing defects in the parent fcc austenite phase and second the exact atomic displacements during the transformation, except the BB/OC model. The BB/OC model helps to analyse the nucleation of the bcc phase at SF (ε-hcp phase). In the present work, we discuss the exact atomic displacements that lead to the fcc-to-bcc martensitic transformation using the MD simulations. Recently transmission electron microscopy (TEM) characterization studies emphasised the presence of preferential nucleation at the twins and SF during the fcc-to-bcc transformation, and the presence of the BB/OC model at the intersection of two ε-hcp phases [12,39]. The TEM studies and the present MD work highlight the importance of considering the effect of pre-existing defects during the martensitic transformation in the existing crystallographic models.

## 5. Conclusions

MD simulations were performed on a semi-empirical EAM potential to study the effect of pre-existing defects on the fcc-to-bcc martensitic transformation. The semi-empirical potential correctly reproduces the negative stacking fault energy (SFE), similar to the first principles data of fcc Fe [29,30]. The type of the defects and their configurations affect the barrier for the atomic motion or shear during crystal structure change.The defect configurations control the transformation mechanisms. These defect structures aid the coordinated movement of the atoms on the favourable slip systems during the martensitic transformation. Fcc crystals with two defect types and three defect configurations were considered in the present work. These defect configurations and their corresponding effect on the fcc-to-bcc crystal structure change is as follows:

(i) Parallel twin boundaries (TB): This system transforms by Nishiyama-Wasserman (NW) mechanism. The atomic shear starts at the TB and thus atoms of the TB aid the transformation.
(ii) Intersecting stacking faults (SF): The crystal structure in this case is a combination of two mechanisms- first the atoms of the SF change from hcp to bcc by Burgers path and then the rest of the fcc atoms follow Burgers-Bogers-Olson-Cohen (BB/OC) mechanism to change from fcc-to-bcc.
(iii) Intersecting TB and SF: This system changes the crystal structure as a combination of previous two cases. The simulation system in this case follows NW, Burgers path, and BB/OC model.

The differences in the transformation temperatures are explained by the analysis of the resolved atomic stresses, $\tau_r$, on the slip systems. This analysis shows that parallel TB have the least barrier for the atomic shear whereas intersecting SF create sessile LC locks and thus have the highest barrier for the atomic shear. The intersecting SF and TB lead to a combination of both the previous cases.

## Acknowledgements

This work received the funding from the European Research Council under the European Unions Seventh Framework Programme FP7/20072013/ERC grant agreement number [306292]. We would like to thank Dr Ralf Meyer at Laurentian University, Canada, for providing us the tabular values of the pure Fe potential. The authors would also like to thank Prof Barend J Thijsse, Astrid Elzas, and Xiaoqin Ou from Delft University of Technology for the useful discussions on this work.

## References

[1] Z. Nishiyama, M. Fine, M. Meshii, C. Wayman (Eds.), Martensitic Transformation, Academic Press, 1978.
[2] E.C. Bain, The nature of martensite, Trans. AIME 70 (1924) 25–35.
[3] Z. Nishiyama, X-ray investigation of the mechanism of the transformation from face-centred to body-centred cubic lattice, Sci. Rep. Tohoku Imp. Univ. 23 (1934) 637–664.
[4] G. Wassermann, K.-W.-I. Mitt, Eisenforsch 17 (1935) 149.
[5] G. Kurdjumow, G. Sachs, Uber den Mechanismus der stahlhärtung, Z. für Phys. 64 (1930) 325–343.
[6] A. Bogers, W. Burgers, Partial dislocations on the {110} planes in the b.c.c. lattice and the transition of the f.c.c. into the b.c.c. lattice, Acta Metall. 12 (1964) 255–261.
[7] G. Olson, M. Cohen, A mechanism for the strain-induced nucleation of martensitic transformations, J. Less Common Met. 28 (1972) 107–118.
[8] C. Cayron, Continuous atomic displacements and lattice distortion during fcc-bcc martensitic transformation, Acta Mater. 96 (2015) 189–202.
[9] H. Bhadeshia, Worked Examples in the Geometry of Crystals, second ed., Institute of Materials, 1987.
[10] D.R. Steinmetz, A Constitutive Model of Twin Nucleation and Deformation Twinning in High-Mn Austenitic TWIP Steels : a Temperature Sensitive Model of Fcc Metals that Twin, Ph.D. thesis, 2013.
[11] J. Venables, The martensite transformation in stainless steel, Phil. Mag. 7 (1962) 35–44.
[12] X.-S. Yang, S. Sun, X.-L. Wu, E. Ma, T.-Y. Zhang, Dissecting the mechanism of martensitic transformation via atomic-scale observations, Sci. Rep. 4 (2014).
[13] G. Krauss, A. Marder, The morphology of martensite in iron alloys, Metall. Trans. 2 (1971) 2343.
[14] D. Pierce, J. Jimnez, J. Bentley, D. Raabe, J. Wittig, The influence of stacking fault energy on the microstructural and strain-hardening evolution of Fe-Mn-Al-Si steels during tensile deformation, Acta Mater. 100 (2015) 178–190.
[15] A. Dumay, J.-P. Chateau, S. Allain, S. Migot, O. Bouaziz, Influence of addition elements on the stacking-fault energy and mechanical properties of an austenitic Fe-Mn-C steel, Mater. Sci. Eng. A 483–484 (2008) 184–187.
[16] C. Sinclair, R. Hoagland, A molecular dynamics study of the fcc-bcc transformation at fault intersections, Acta Mater. 56 (2008) 4160–4171.
[17] X. Ou, J. Sietsma, M.J. Santofimia, Molecular dynamics simulations of the mechanisms controlling the propagation of bcc/fcc semi-coherent interfaces in iron, Model. Simul. Mater. Sci. Eng. 24 (2016) 055019.
[18] B. Wang, H.M. Urbassek, Phase transitions in an Fe system containing a bcc/fcc phase boundary: an atomistic study, Phys. Rev. B 87 (2013) 104108.
[19] C. Bos, J. Sietsma, B.J. Thijsse, Molecular dynamics simulation of interface dynamics during the fcc-bcc transformation of a martensitic nature, Phys. Rev. B 73 (2006) 104117.
[20] B. Wang, E. Sak-Saracino, N. Gunkelmann, H.M. Urbassek, Molecular-dynamics study of the $\gamma < - > \alpha$ phase transition in Fe-C, Comput. Mater. Sci. 82 (2014) 399–404.
[21] R. Meyer, P. Entel, Martensite-austenite transition and phonon dispersion curves of Fe$_{1-x}$Ni$_x$ studied by molecular-dynamics simulations, Phys. Rev. B 57 (1998) 5140–5147.
[22] C. Engin, L. Sandoval, H.M. Urbassek, Characterization of Fe potentials with respect to the stability of the bcc and fcc phase, Model. Simul. Mater. Sci. Eng. 16 (2008) 035005.
[23] P. Entel, R. Meyer, K. Kadau, H. Herper, E. Hoffmann, Martensitic transformations: first-principles calculations combined with molecular-dynamics simulations, Eur. Phys. J. B Cond. Matter Complex Syst. 5 (1998) 379–388.
[24] P. Entel, R. Meyer, K. Kadau, Molecular dynamics simulations of martensitic transitions, Phil. Mag. B 80 (2000) 183–194.
[25] L. Sandoval, H.M. Urbassek, P. Entel, The Bain versus Nishiyama-Wassermann path in the martensitic transformation of Fe, New J. Phys. 11 (2009) 103027.
[26] W. Pepperhoff, M. Acet, Constitution and Magnetism of Iron and its Alloys, Springer, 2001.
[27] E. Sak-Saracino, H.M. Urbassek, Temperature-induced phase transformation of Fe$_{1\text{-}x}$Ni$_x$ alloys: molecular-dynamics approach, Eur. Phys. J. B 88 (2015) 1–9.
[28] H. Song, J. Hoyt, A molecular dynamics study of heterogeneous nucleation at grain boundaries during solid-state phase transformations, Comput. Mater. Sci. 117 (2016) 151–163.
[29] A. Dick, T. Hickel, J. Neugebauer, The effect of disorder on the concentration-dependence of stacking fault energies in Fe$_{1-x}$Mn$_x$ - a first principles study, Steel Res. Int. 80 (2009) 603–608.
[30] I. Bleskov, T. Hickel, J. Neugebauer, A. Ruban, Impact of local magnetism on stacking fault energies: a first-principles investigation for fcc iron, Phys. Rev. B 93 (2016) 214115.
[31] T. Lee, M.I. Baskes, S.M. Valone, J.D. Doll, Atomistic modeling of thermodynamic equilibrium and polymorphism of iron, J. Phys. Cond. Matter 24 (2012) 225404.
[32] F. Maresca, W. Curtin, The austenite/lath martensite interface in steels:

structure, athermal motion, and in-situ transformation strain revealed by simulation and theory, Acta Mater. 134 (2017) 302–323.

[33] R. Meyer, P. Entel, Lattice dynamics of martensitic transformations examined by atomistic simulations, Phys. IV 7 (1997) C5–C29.

[34] P. Wang, S. Xu, J. Liu, X. Li, Y. Wei, H. Wang, H. Gao, W. Yang, Atomistic simulation for deforming complex alloys with application toward TWIP steel and associated physical insights, J. Mech. Phys. Solids 98 (2017) 290–308.

[35] S. Plimpton, Fast parallel algorithms for short-range molecular dynamics, J. Comput. Phys. 117 (1995) 1–19.

[36] A. Stukowski, Visualization and analysis of atomistic simulation data with OVITO- the open visualization tool, Model. Simul. Mater. Sci. Eng. 18 (2010) 015012.

[37] J. Hirth, J. Lothe, Theory of Dislocations, 1981.

[38] R.P. Reed, A.F. Clark, Advances in Cryogenic Engineering Materials, vol. 28, Plenum Press, Newyork and London, 1981.

[39] Y. Shen, X. Li, X. Sun, Y. Wang, L. Zuo, Twinning and martensite in a 304 austenitic stainless steel, Mater. Sci. Eng. A 552 (2012) 514–522.